2. GLOBAL CLIMATE—

A. M. Waple, Ed.[89]

a. Overview

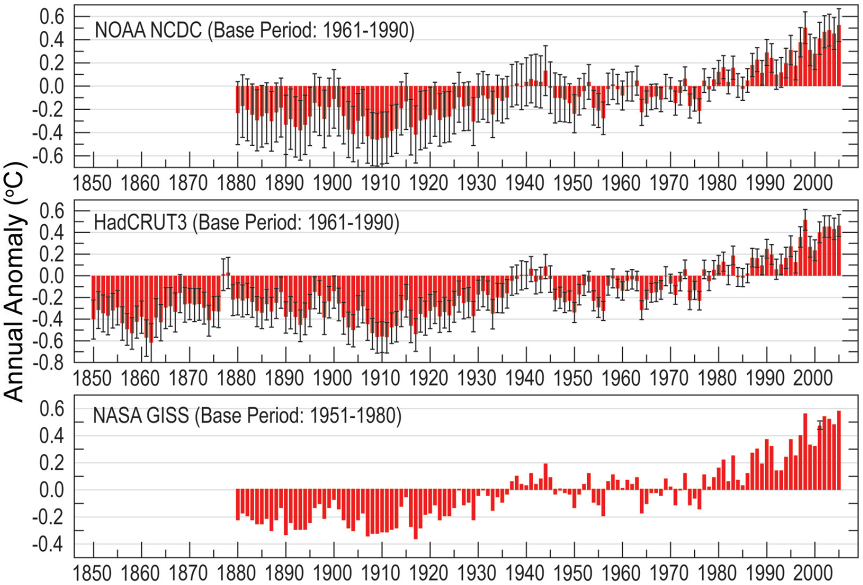

Fig. 2.1. Global annual surface temperature departures (°C) from the 1961 to 1990 average. The 95% confidence limits for the annual global estimates are shown (black error bars). [Sources: NOAA/NCDC; The Hadley Centre for Climate Prediction and Research and the Climatic Research Unit of the University of East Anglia; and NASA GISS]

The year 2005 was notable for its global warmth, both at the surface and throughout the troposphere. Globally, surface temperature remained above average in all 12 months and reached a record high value for the year. This anomalous warmth is part of a long-term warming trend of approximately 0.7°C century^{-1} since 1900, and a rate of increase almost three times as great since 1976. This section provides a summary of tropospheric and surface global temperatures and outlines the differences between the three main surface datasets used to calculate global temperature. Also, below-average stratospheric temperatures in 2005, consistent with a stratospheric cooling trend, are discussed.

Global average precipitation in 2005 was near the long-term mean, with some regions wetter, and some drier than normal. Snow cover was below average across much of the Northern Hemisphere for the year, consistent with the anomalously warm surface temperatures. Global carbon dioxide (CO_2) concentration rose in 2005 by about 2 parts per million (ppm) to 378.9 ppm, which is an increase slightly above the +1.6 ppm yr^{-1} observed since 1980.

b. Global temperature

1) Surface temperature—M. J. Menne[55]

The global annual average surface temperature in 2005 was at or near record high levels according to analysis conducted independently at institutions in the United Kingdom (Hadley Centre of the Met Office and the Climate Research Unit of the University of East Anglia) and in the United States [NOAA's National Climatic Data Center and the National Aeronautics and Space Administration's (NASA's) Goddard Institute for Space Studies (GISS)]. As shown in Fig. 2.1, the value for 2005 ranks as highest on record according to the NOAA and NASA analyses and second highest, behind 1998, according to the Met Office's Hadley Centre/University of East Anglia's Climate Research Unit analysis. However, when uncertainties related to estimating the global mean are considered, the two highest annual values are effectively indistinguishable from one another. Based on the NOAA/NCDC record, the rise in global surface temperatures since 1900 is 0.66°C, when calculated as a linear trend.

Record high monthly global averages were observed in April, May, June, and September 2005 (Fig. 2.2). Figure 2.2 indicates that global surface temperature values in 2005 were sustained at levels near the 1998 values, but without the influence of a

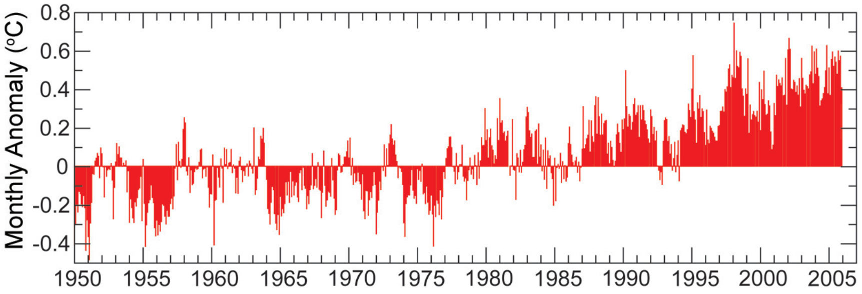

Fig. 2.2. Serial monthly surface temperature anomalies (°C) relative to a 1961–90 base period, based on Quayle et al. (1999). [Source: NOAA/NCDC]

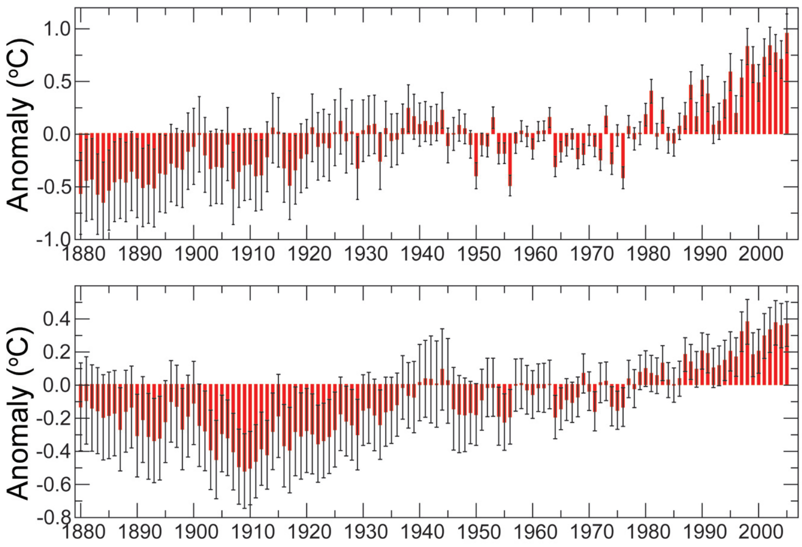

Fig. 2.3. Sea surface and land surface temperature anomalies (°C) with respect to the 1961–90 mean. [Source: NOAA/NCDC]

strong El Niño–Southern Oscillation (ENSO) warm event like that which occurred in 1997/98.

Global land surface temperatures ranked highest on record according to the NOAA/NCDC record, while sea surface temperatures ranked third highest (Fig. 2.3), behind 1998 and 2003. Many regions across the globe recorded temperatures well in excess of the 1961–90 mean (Fig. 2.4). In some areas, most notably throughout much of the North Atlantic basin, the average for 2005 exceeded the 90th or 98th percentiles of the mean annual temperature distribution (Fig. 2.5) estimated using 1961–90 observations (Horton et al. 2001). These anomalies are discussed in more detail in the tropical cyclones section (see section 4c). Averaged separately by hemisphere, 2005 surface temperatures rank as second highest in the NH and as sixth highest in the SH according to the NOAA/NCDC archive.

Regionally, 2005 temperatures were highest on record in Australia. High average temperatures were also observed across much of Canada and Siberia. An intense heat wave occurred across India, Pakistan, and Bangladesh in May and June. Conversely, cold conditions were experienced across much of Europe and North Africa in February. These events are discussed in detail in the regional climate sections (see section 6).

ii) Upper-air tropospheric temperatures—J. C. Christy[17]

The temperature variations of three broad atmospheric layers, the low to middle troposphere (LT: surface–300 hPa), the middle troposphere to lower stratosphere (MT: surface–70 hPa), and the upper troposphere to lower stratosphere (LS: 150–20 hPa) are presented. Products from two radiosonde-based datasets—Radiosonde Atmospheric Temperature Products for Analysis of Climate (RATPAC; Free et al. 2005) based on 85 stations, and Hadley Atmospheric Temperatures (HadAT2; Thorne et al. 2005) based on about 650 stations—are included in the data. Satellite products are of the LT, MT, and LS from the University of Alabama in Huntsville (UAH; Christy et al. 2003) and of the MT and LS from Remote Sensing Systems (RSS; Mears et al. 2003).

The annual LT temperature anomaly for 2005 was second warmest (tied for second in UAH) since either radiosonde (1958) or satellite (1979) records began (Fig. 2.6). The warmest calendar year remains 1998[1]. The anomaly correlations are extremely high

---

[1] Note that global and tropical tropospheric temperatures tend to lag surface temperatures by about 6 months, meaning the phase of the ENSO warmth was shifted further into 1998 for upper air relative to that which was measured at the surface.

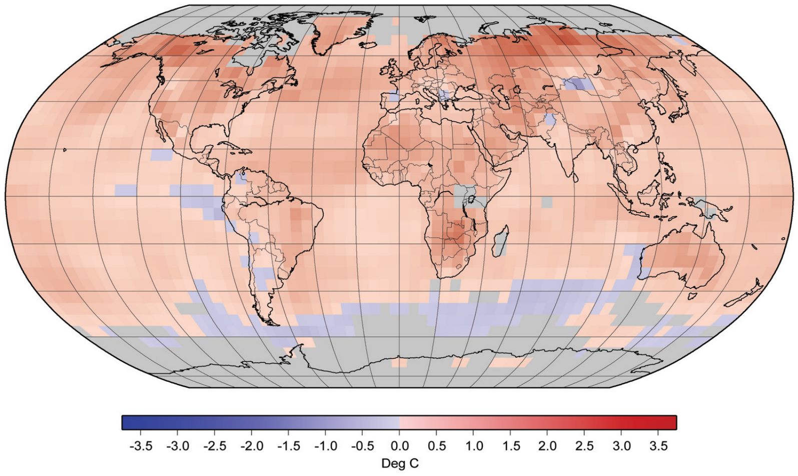

Fig. 2.4. Geographic distribution of surface air temperature anomalies (°C) in 2005 relative to the 1961–90 mean. [Source: NOAA/NCDC]

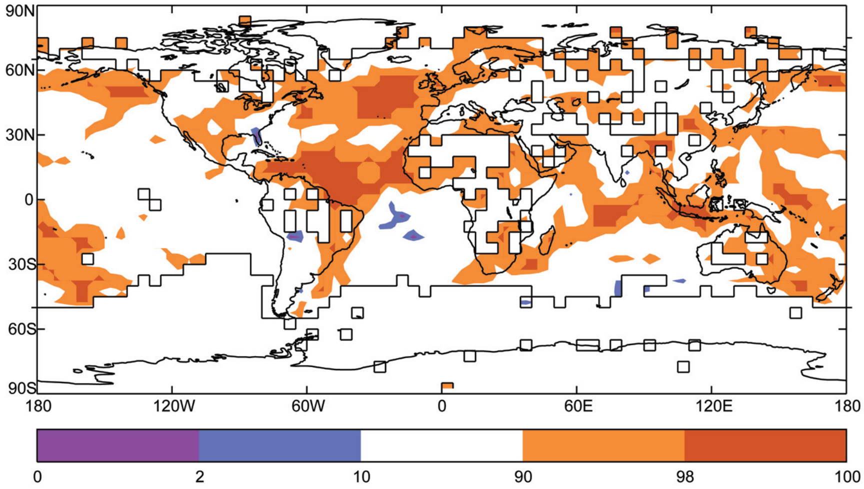

Fig. 2.5. Land surface temperature anomalies (°C) based on HadCRUT3 expressed as percentiles of modified two-parameter gamma distributions fit to annual data for 1961–90 according to Horton et al. (2001). [Source: Hadley Centre for Climate Prediction and Research]

among the datasets, but the linear trend reveals slight differences since 1979 (Table 2.1). The largest trends in all datasets are found in the northern third of the globe. A visual interpretation of long-term change suggests a relatively strong increase in global temperatures around 1978 and another shift to warmer temperatures associated with the 1997/98 ENSO. The base period for the plot is 1979–98, and since 1977, no seasonal anomaly has dipped below –0.4°C. Since 1998, only one dataset has dipped below –0.1°C.

The northern polar region (60°–85°N) experienced its warmest annual reading in the period of record (+1.3°C). No large-scale region had an annual mean negative anomaly relative to the 1979–98 base period, although smaller areas did.

The MT layer (Fig. 2.7), which includes some stratospheric influence, presents a similar picture. However, while 2005 was the second warmest globally for the two radiosonde datasets, it was fourth and fifth warmest in the RSS and UAH satellite datasets, respectively. Linear trends in MT are more negative than LT, because the cooling stratosphere exerts an influence on MT (Table 2.1).

The quasi-biennial oscillation (QBO) was in the easterly phase in 2005 and contributed to a tropical (20°N–20°S) anomaly that was the coldest on record in the stratosphere. The 2005 global annual anomaly was near those of 1995, 1996, and 2000 in the satellite records (Fig. 2.8), but was not the coldest. Linear trends are more variable among the datasets, but all indicate significant cooling over the period (Table 2.1). However, since about 1995, global trends have been near zero (Fig. 2.8).

High-latitude LS anomalies were exceptionally cold in a broad area centered over Greenland, but were warmer than average over eastern Antarctica. The coldest large-scale monthly anomalies occurred over the NH polar region in January and February (-6°C, 60°–85°N), while the warmest monthly

Table 2.1. Linear trends (°C decade^{-1}) from 1979 to 2005 of global and tropical (20°S–20°N) anomalies for the three temperature products. 1958–2005 trends in parentheses.

	RATPAC	HadAT2	UAH	RSS
Global LT	+0.15 (+0.15)	+0.17 (+0.15)	+0.13*	
Tropical LT	+0.11 (+0.13)	+0.09 (+0.13)	+0.07	
Global MT	+0.04 (+0.08)	+0.06 (+0.09)	+0.05	+0.14
Tropical MT	+0.02 (+0.08)	+0.01 (+0.09)	+0.06	+0.15
Global LS	–0.71 (–0.42)	–0.57 (–0.36)	–0.45	–0.32
Tropical LS	–0.75 (–0.45)	–0.60 (–0.34)	–0.41	–0.29

* When subsampled at 50°–85°N to more closely represent the geographical extent of HadAT2, UAH LT "global" trend is +0.15°C decade^{-1}.

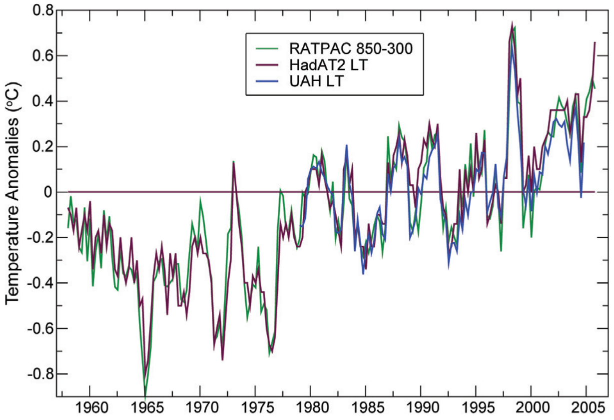

Fig. 2.6. Seasonal anomalies (°C) of global average lower-tropospheric layer temperature. HadAT2, UAH, and RSS depict the temperature of layers representing the microwave brightness temperature weighting functions (roughly surface to 300 hPa, peaking around 700 hPa), while RATPAC depicts the 850–300-hPa layer mean temperature.

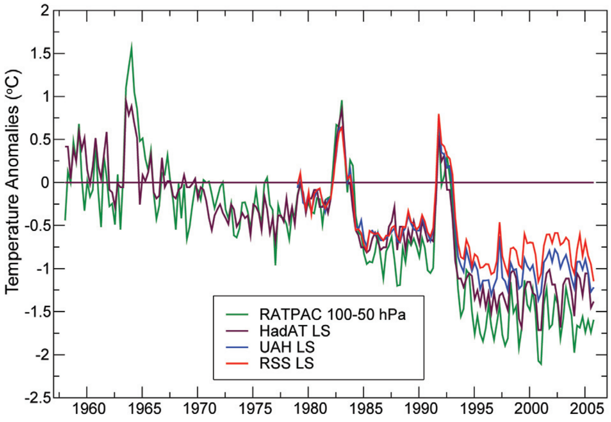

Fig. 2.8. Seasonal anomalies (°C)of global lower-stratospheric temperature. This layer begins around 120 hPa and diminishes above 20 hPa. RATPAC data depict anomalies of the 100–50-hPa layer.

anomalies (+2°C) appeared over the SH polar region in October and November. This marks the fourth year in a row where anomalies of the SH polar region were above average (1979–98) for austral spring in satellite records (see section 5c).

c. *Hydrologic cycle*

1) Global precipitation

(i) Land—D. H. Levinson,[46] J. H. Lawrimore,[45] and D. B. Wuertz[94]

Global precipitation anomalies determined from land-based gauges were analyzed on both an annual and a seasonal basis using data from the Global Historical Climatology Network (GHCN; Peterson and Vose 1997). Anomalies over the period of 1901–2005 were determined from the GHCN dataset with respect to the 1961–90 mean using those stations with a minimum of 20 years of data during the base period (Peterson and Vose 1997; Vose et al. 1992). Global precipitation was average in 2005, with an annual anomaly less than 1 mm (−0.87 mm) below the 1961–90 mean (Fig. 2.9a).

Over the past two-and-a-half decades, global precipitation has been generally below the long-term mean, with above-average precipitation anomalies in only 7 of the last 25 years. This multidecadal period of below-normal precipitation and anomalously dry conditions began during the early 1980s, and has continued through the 1990s into the present decade. The peak in this dry period appears to have occurred in 1992, corresponding with a multiyear El Niño event. Previous studies (i.e., Ropelewski and Halpert 1987) have shown that variability associated with ENSO influences large-scale precipitation patterns in the Tropics and midlatitudes, both of which contribute to generally drier conditions at high latitudes.

Regardless of the potential causes of the multidecadal dry period, much of the observed signal in global precipitation anomalies appears to be seasonally dependent (Figs. 2.9b–e). In 2005, negative anomalies were observed in three of the four seasons, with only the boreal autumn [September–November (SON)] having above-average precipitation for the year. During this extended dry period, below-normal precipitation occurred primarily during two seasons [March–May (MAM) and June–August (JJA)], with the boreal summer having the longest continuous

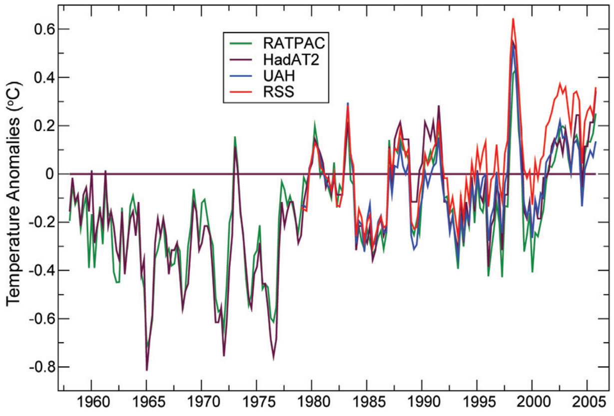

Fig. 2.7. Seasonal anomalies (°C) of global average tropospheric temperature. This layer includes a portion of the lower stratosphere, representing a microwave brightness temperature weighting function that starts at the surface, peaks in the midtroposphere, and diminishes rapidly above 100 hPa.

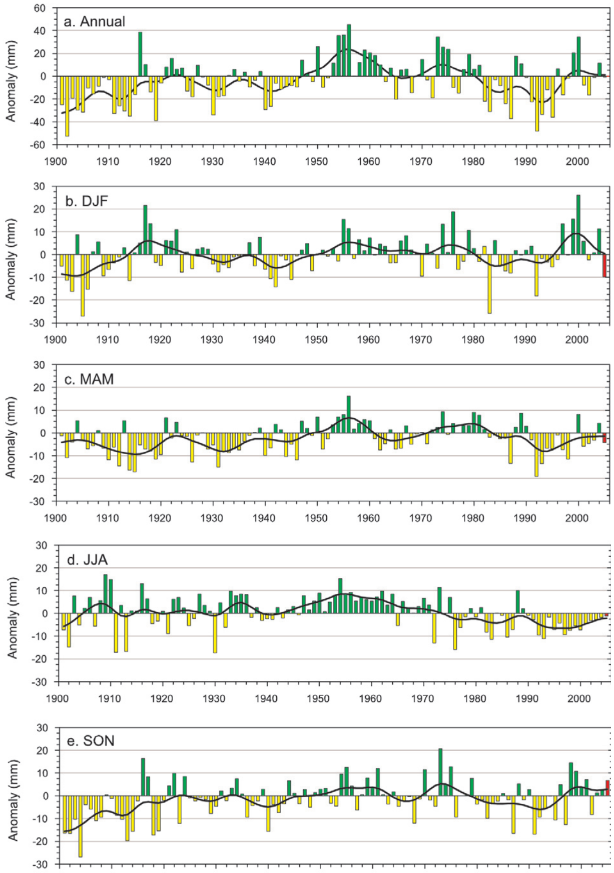

Fig. 2.9. Time series of annual and seasonal global precipitation anomalies over the period 1901–2005, with observations from the GHCN dataset: a) annual, b) December–February (DJF), c) MAM, d) JJA, and d) SON. The precipitation anomalies were calculated in mm with respect to the 1961–90 base period mean: green bars = positive anomalies, yellow bars = negative anomalies, and red bar = 2005 anomaly. In addition, the black line in each time series denotes the smoothed annual or seasonal values using a 13-point binomial filter.

period of drier-than-normal conditions, extending from the late 1980s through 2005.

For the first half of the twentieth century, and extending into the 1960s, much of the Tropics in the NH were dominated by wet precipitation anomalies, while midlatitude regions in both hemispheres were drier than normal (Fig. 2.10). It is likely that the period of dry anomalies in the northern high-latitudes during 1900–40 was due to a lack of precipitation data, as well as a systematic undercatch of snow and solid precipitation. Since the 1960s, there has been an extended period of dry anomalies in the Tropics, particularly in the NH. In recent years, including 2005, high-latitude regions of the NH have been wetter than normal, with a multiyear wet period north of 60°N.

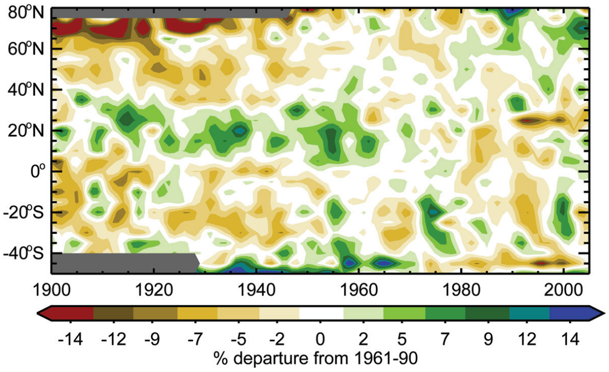

Fig. 2.10. Hovmoeller plot of the percentage departure from 1961 to 1990 means of GHCN global annual precipitation, with zonal means determined over 5° latitude bands and covering the period 1900–2005. A 13-point binomial filter was applied to each zonal time series, with green and blue shades corresponding to wet anomalies and red and brown shades corresponding to dry anomalies. Gray shading in the early twentieth century is due to a lack of data in high-latitude regions.

Significant precipitation anomalies were observed at many long-term monitoring locations over the past year (Fig. 2.11), but several regions stand out as being either significantly wetter or drier than normal. Of special note were the large dry anomalies in parts of East Asia, particularly across southern Japan, eastern China, and the Korean Peninsula, in part due to below-normal number of landfalling tropical cyclones (see section 4c). Other regions with significant dry anomalies included much of Australia, South Africa and coastal areas of the Gulf of Guinea, the Iberian Peninsula and France, and a large portion of the central United States, extending from the Gulf of Mexico to the Great Lakes. Locations significantly

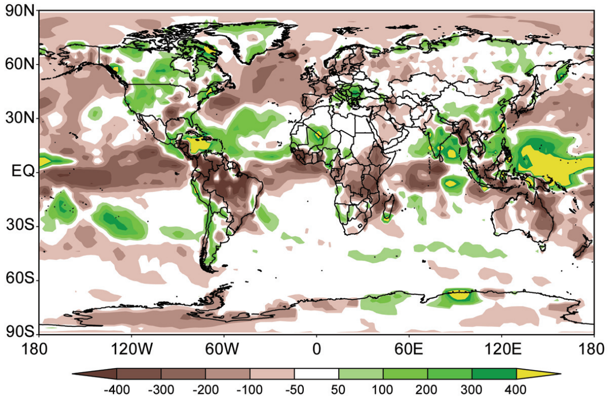

Fig. 2.11. Precipitation anomalies (mm) relative to a 1970–2000 base period from the gauge–satellite merged CAMS–OPI precipitation dataset (Janowiak and Xie 1999).

wetter than average in 2005 included most of Scandinavia, Senegal and the Atlantic coast of West Africa, Venezuela and Columbia, and a large portion of the Caribbean basin. Further details on these and other regional precipitation anomalies can be found in section 6.

(ii) Oceans—P. Xie[95] and J. E. Janowiak[34]

Real-time monitoring of global oceanic precipitation is routinely conducted at NOAA's Climate Prediction Center (CPC) with the use of the gauge–satellite merged Climate Anomaly Monitoring System (CAMS)–outgoing longwave radiation (OLR) Precipitation Index (OPI) dataset (Janowiak and Xie 1999). By combining the gauge observations of precipitation collected and archived by CPC via CAMS (Ropelewski et al. 1985) with the satellite-based OPI (Xie and Arkin 1998), CAMS–OPI provides monthly precipitation estimates over global land and ocean on a real-time basis.

Global oceanic precipitation during 2005 is characterized by rainbands associated with the intertropical convergence zone (ITCZ), South Pacific convergence zone (SPCZ), and the midlatitude oceanic storm tracks (Fig. 2.12). Mean precipitation over the entire global ocean during 2005 was 2.840 mm day^{-1}, equivalent to a freshwater influx of 1036.6 kg m^{-2}. Maximum annual precipitation rates of over 10 mm day^{-1} were observed during the year over the tropical western Pacific where the ITCZ merges with the SPCZ (see section 4d). Meanwhile, relatively light precipitation occurred over several oceanic dry zones of the southeast Pacific, northeast Pacific off the coast of the southwest United States, southeast Atlantic, tropical North Atlantic near western Africa, and the eastern Indian Ocean.

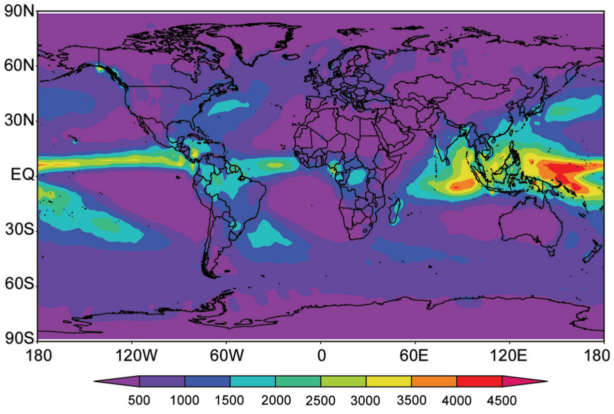

Fig. 2.12. Precipitation totals (mm) for 2005 from the gauge–satellite merged CAMS–OPI precipitation dataset (Janowiak and Xie 1999).

The distribution of precipitation anomalies during 2005 indicates a dipole pattern of wet and dry anomalies over the western and eastern tropical Pacific, respectively (Fig. 2.11). Although weak El Niño conditions prevailed over the tropical Pacific in the second half of 2004 and continued into early 2005 (Lyon and Barnston 2005; see also section 4b), enhanced precipitation was limited mostly to the tropical Pacific west of the date line. This pattern is different from that typical of a medium or strong El Niño event when large positive precipitation anomalies occur over the central and eastern Pacific (Ropelewski and Halpert 1989; Xie and Arkin 1997).

Enhanced convection, and attendant above-normal precipitation, was first observed in late 2004 over the tropical western Pacific north of Indonesia (Fig. 2.13). The positive precipitation anomaly intensified as it moved eastward, and reached its maximum intensity during January–March of 2005. Such large intraseasonal variations present in Fig. 2.13 are associated with the strong MJO (Madden and Julian

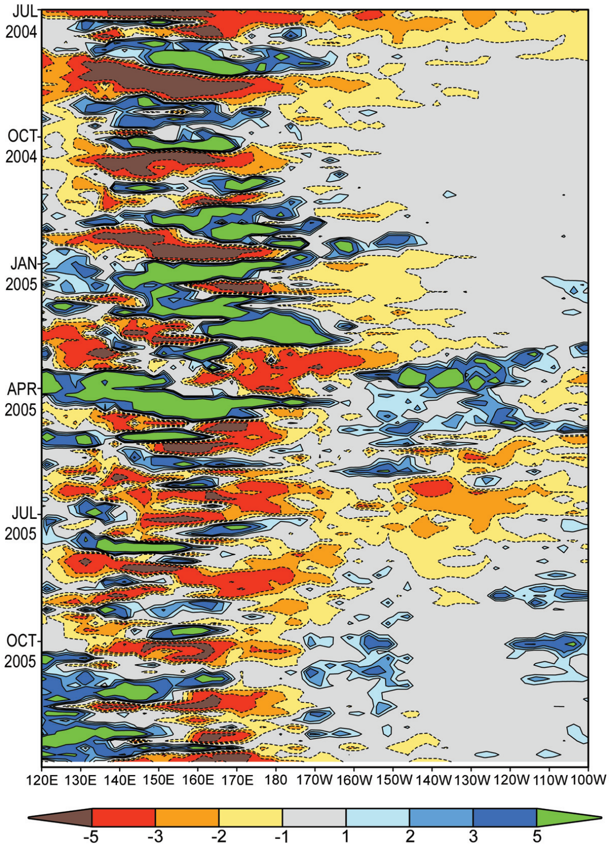

Fig. 2.13. Time–longitude section of precipitation anomaly (mm; 1979–95 base period) averaged over the tropical Pacific (5°S–5°N) as observed by the Global Precipitation Climatology Project (GPCP) pentad precipitation dataset (Xie et al. 2003).

1971) activity that was observed during that period (Climate Prediction Center 2005). The positive precipitation anomaly over the tropical western Pacific gradually shifted westward during the second half of 2005 as the coupled ocean–atmosphere system evolved toward a weak La Niña.

A substantial positive precipitation anomaly was observed over regions of strong hurricane activity in the Atlantic basin, especially the Caribbean Sea (see section 4c). The Atlantic ITCZ was located slightly north of its climatological latitude, which is reflected by two parallel bands of positive and negative precipitation anomalies over the tropical Atlantic (Fig. 2.11).

Substantially depressed precipitation over the northwestern Atlantic during 2005 also was noticeable. Examination of monthly precipitation and atmospheric circulation fields suggest that the bulk of the negative precipitation anomaly over the region was the result of below-normal winter storm activity in the oceanic storm track, which is a climatological feature over the western North Atlantic during the cool season. This reduced storminess was associated with strong anticyclonic blocking activity over the high latitudes that was observed during the winter season.

ii) Snow—D. A. Robinson[75]

Annual snow cover extent (SCE) over NH lands averaged 24.7 million km^2 in 2005. This is 0.9 million km^2 less than the 36-yr average and ranks 2005 as having the 32nd most extensive cover of record (Table 2.2). This evaluation includes snow over the continents, including the Greenland Ice Sheet. The SCE in 2005 ranged from 47.6 million km^2 in February to 2.3 million km^2 in August. Monthly snow extent values are calculated at the Rutgers Global Snow Laboratory from weekly SCE maps produced by NOAA meteorologists, who rely primarily on daily visible satellite imagery to construct the maps.

Hemispheric SCE was only above the long-term mean in February, March, and December; thus, the 12-month running means of NH extent were below the long-term average throughout the year (Fig. 2.14). This has almost exclusively been the situation since the late 1980s. Eurasian SCE was somewhat below the long-term average in 2005 and ranked as the 25th most extensive cover of the satellite era. North American SCE was much below average, ranking 35th (Figs. 2.15 and 2.16).

As is common, 2005 SCE showed significant spatial and temporal variability. For instance, hemi-

Table 2.2. Monthly and annual climatological information for NH and continental snow extent between November 1966 and December 2005. Included are the numbers of years with data used in the calculations, means, standard deviations, 2005 values, and rankings. Areas are in millions of km^2. 1968, 1969, and 1971 have 1, 5, and 3 missing months, respectively, and thus are not included in the annual (Ann) calculations. North America includes Greenland.

	Yrs	Mean	Std dev	2005	2005 NH rank	Eurasia rank	North American rank
Jan	39	46.9	1.5	46.7	21	27	15
Feb	39	45.9	1.9	47.6	9	3	33
Mar	39	41.0	1.9	41.3	18	12	25
Apr	39	31.4	1.7	29.9	31	20	38
May	39	20.5	1.9	17.6	38	36	38
Jun	38	11.0	2.1	9.0	31	31	30
Jul	36	4.9	1.4	3.0	36	33	35
Aug	37	3.5	1.0	2.3	37	33	37
Sep	37	5.7	1.0	4.8	31	33	21
Oct	38	18.3	2.6	16.9	31	24	34
Nov	40	34.1	2.1	32.2	32	30	31
Dec	40	43.5	1.8	44.5	10	11	13
Ann	36	25.6	1.0	24.7	32	25	35

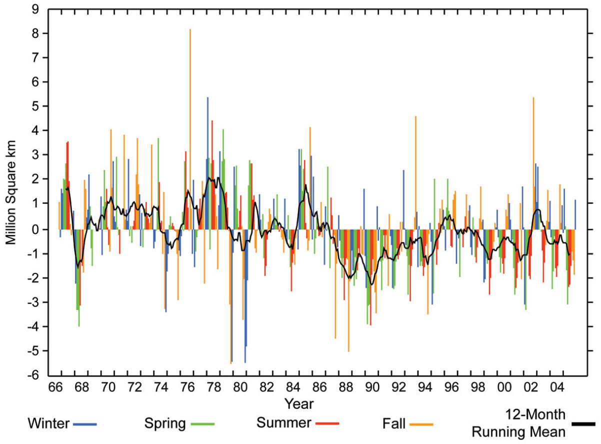

Fig. 2.14. Anomalies of monthly snow cover extent over Northern Hemisphere lands (including Greenland) between Nov 1966 and Dec 2005, calculated from NOAA snow maps. Also shown are 12-month running mean anomalies of hemispheric snow extent, plotted on the seventh month of a given interval. Mean hemispheric snow extent is 25.6 million km^2 for the full period of record. Monthly means for the period of record are used for nine missing months between 1968 and 1971 in order to create a continuous series of running means. Missing months fall between June and October; no winter months are missing.

spheric SCE ranked in the top 10 in February and December, while totals ranked in the lowest 10 from April through November. February's NH anomaly was positive due to the Eurasian extent being the third largest on record, despite North America ranking 33rd. December's high ranking was the result of extensive cover over both continents; this followed November, when both ranked quite low. Spring snow cover continues to be less extensive in the second half of the satellite record than in the first half. Lower-than-average North American SCE was first noted in February, while well-below-average Eurasian cover did not occur until May.

Over the contiguous United States, end-of-winter SCE was very low after February, while in Alaska, May SCE was at a record low. Both regions began the boreal fall snow season slowly, especially in Alaska, where SCE was at a record low in September and only increased to second lowest in October and third lowest in November, resulting in a very long snow-free season for 2005 in Alaska.

Maps depicting daily, weekly, and monthly conditions, daily and monthly anomalies, and monthly climatologies for the entire period of record may be viewed at the Rutgers Global Snow Laboratory Web site (available online at http://climate.rutgers.edu/snowcover).

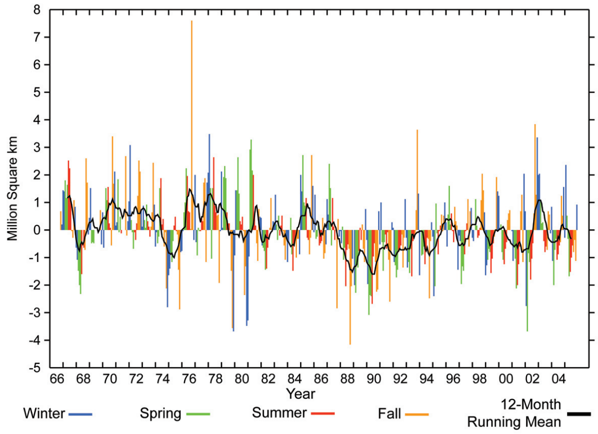

Fig. 2.15. Same as Fig. 2.14, except for Eurasia.

d. Trace gases

1) Carbon dioxide—R. C. Schnell[81]

Carbon dioxide emitted from natural and anthropogenic (i.e., fossil fuel combustion) sources is partitioned into three mobile reservoirs: atmosphere, oceans, and the terrestrial biosphere. The result of increased fossil fuel combustion has been that atmospheric CO_2 has increased from about 280 ppm (parts in 10^6 by dry-air mole fraction) at the start of the industrial revolution to about 380 ppm today (Fig. 2.17a). Roughly half the emitted CO_2 remains in the atmosphere and the remainder has gone into two "sinks"–oceans and the land biosphere (which includes plants and soil carbon).

The present rate of anthropogenic carbon emission to the atmosphere is nearly 7 Pg yr^{-1} (Pg = 10^{15} g). During the 1990s, net uptake by the oceans was estimated at 1.7 ±0.5 Pg yr^{-1}, and by the land biosphere

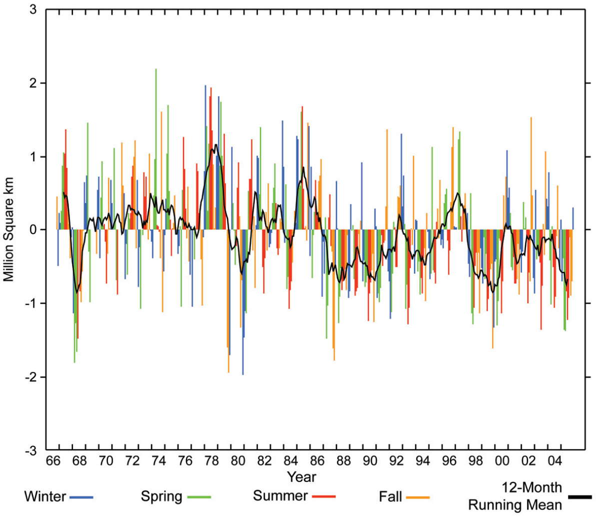

Fig. 2.16. Same as Fig. 2.14, except for North America (including Greenland).

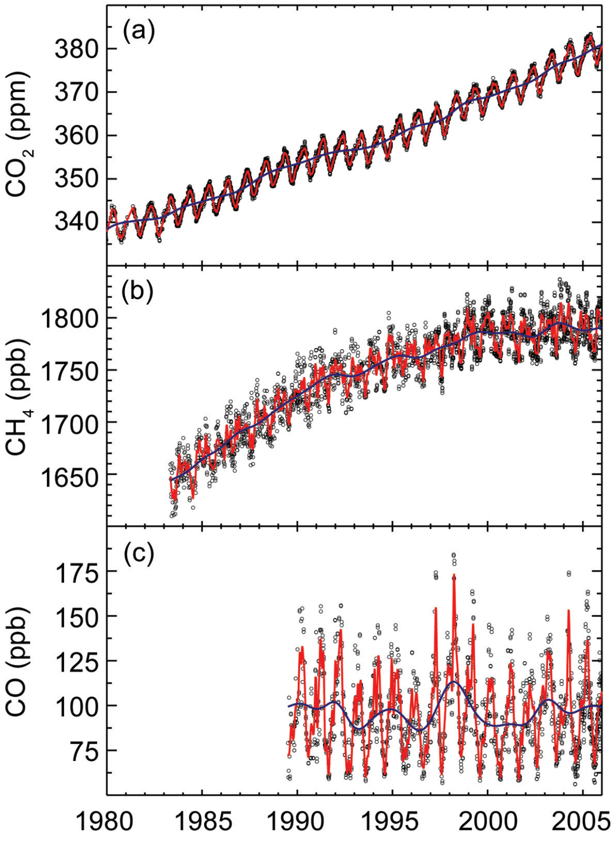

Fig. 2.17. Trace gas mole fractions (black symbols) determined from samples collected at the NOAA ESRL Mauna Loa Observatory (MLO) for (a) CO_2 (courtesy: T. J. Conway, NOAA). Current trends at MLO and globally averaged are available online at www.cmdl.noaa.gov/ccgg/trends/. (b) CH_4 (courtesy: E. J. Dlugokencky, NOAA), and (c) CO (courtesy: P. C. Novelli, NOAA). In all panels, the solid blue line is the deseasonalized trend and the red line is a smooth curve fitted to the black symbols. More plots can be found online at www.cmdl.noaa.gov/ccgg.

as 1.4 ±0.7 Pg yr^{-1} (Prentice et al. 2001). The gross atmosphere–ocean and atmosphere–terrestrial biosphere (i.e., photosynthesis and respiration) fluxes are on the order of 100 Pg yr^{-1}. Interannual variations in the atmospheric increase of CO_2 (Fig. 2.17a; based on Conway et al. 1994) are not attributed to variations in fossil fuel emissions, but rather to small changes in these net fluxes. Most attempts to explain the interannual variability of the atmospheric CO_2 increase have focused on short-term climate fluctuations (e.g., ENSO and post–Mt. Pinatubo cooling), but the mechanisms, especially the role of the terrestrial biosphere, are poorly understood. To date, about 5% of conventional fossil fuels have been combusted. If combustion were stopped today, it is estimated that after a few hundred years, 15% of the total carbon emitted would remain in the atmosphere, and the remainder would be in the oceans.

In 2005, the globally averaged atmospheric CO_2 mole fraction was 378.9 ppm, just over a 2 ppm increase from 2004. This continues the steady upward trend in this abundant and long-lasting greenhouse gas. Since 1900, atmospheric CO_2 has increased 84 ppm (22%), with an average annual increase of 1.6 ppm since 1980.

In calculating the global mean mole fractions of CO_2 and other trace gases, the number of stations varies through time and may be different for each gas at any point in the period of record. Each record is temporally smoothed, with evenly spaced values selected from these temporal fits to generate new fits as a function of latitude (ϕ). Values extracted from the latitude fit at a spacing of $\sin(\phi) = 0.05$ (i.e., at equal atmospheric volumes) define a matrix of species value as a function of time and latitude. These are then used to calculate global averages at weekly and annual time resolution (Conway et al. 1994).

ii) Methane—R. C. Schnell[81]

Methane's (CH_4) contribution to anthropogenic radiative forcing, including direct and indirect effects, is about 0.7 W m^{-2}, or roughly half that of CO_2. Also, changes in the burden of CH_4 feed back into atmospheric chemistry, affecting the concentrations of hydroxyl (OH) and ozone (O_3). The increase in CH_4 since the preindustrial era is responsible for about half of the estimated increase in background tropospheric O_3 during that time. Changes in OH concentration affect the lifetimes of other greenhouse gases such as hydrochlorofluorocarbons (HCFCs) and hydrofluorocarbons (HFCs).

High-precision measurements of atmospheric CH_4 provide climate modelers with current and past rates of CH_4 increase, and they are also useful in constraining the CH_4 budget. During 20 years of measurements, CH_4 has increased, but the rate of increase has slowed in recent years (Fig. 2.17b). A large increase in 1998 was likely the result of climatic conditions that resulted in increased emissions from wetlands and biomass burning. Measurements of CH_4 at Mauna Loa, Hawaii, remained nearly constant from 1999 to 2002 (Dlugokencky et al. 2003). In 2003, CH_4 increased by about 5 ppb (parts in 10^9 by dry-air mole fraction), primarily due to increases in the Northern Hemisphere. This was followed by a small decrease in 2004, and little change from those levels in 2005. Globally averaged CH_4 in 2005 was 1774.8 ppb, which represented a decrease of 2.8 ppb from 2004.

iii) Carbon monoxide—R. C. Schnell[81]

Unlike CO_2 and CH_4, carbon monoxide (CO) does not strongly absorb terrestrial infrared radiation, but does impact climate through its chemistry. The chemistry of CO affects OH (which influences the lifetimes of CH_4 and HFCs) and tropospheric O_3 (itself a greenhouse gas), so emissions of CO can be considered equivalent to emissions of CH_4 (Prather 1996). Current emissions of CO may contribute more to radiative forcing over decadal time scales than emissions of anthropogenic nitrous oxide (N_2O; Daniel and Solomon 1998).

Carbon monoxide mole fractions from Mauna Loa (Fig. 2.17c, symbols) show little trend over the measurement period (updated from Novelli et al. 2003). Superimposed on the flat trend is a significant increase during 1997 and 1998, which was likely the result of tropical (Langenfelds et al. 2002) and boreal biomass burning (Kasischke et al. 2000). Because the lifetime of CO is relatively short (a few months), the anomaly quickly disappeared and CO quickly returned to pre-1997 levels. Carbon monoxide levels in 2005 were comparable to those found in the early 2000s. The globally averaged CO mole fraction in 2005 was 83.5 ppb, very near the average of the past five years. Since 1991, little trend in globally averaged CO has been observed.

iv) Nitrous oxide and sulfur hexaflouride—
J. W. Elkins[21] and G. S. Dutton[20]

Atmospheric N_2O and sulfur hexafluoride (SF_6) are present in lower concentrations than CO_2, but the radiative forcing of each is far greater. Nitrous oxide is the third strongest greenhouse gas, while each SF_6 molecule is 22,200 times more effective as an infrared absorber than one CO_2 molecule, and has an atmospheric lifetime of between 500 and 3200 years. The concentration of both species has grown at a linear rate, N_2O at 0.76 ppb yr^{-1} (0.25% yr^{-1}) since 1978 (Fig. 2.18a) and SF_6 at a rate of 0.22 ppt (parts in 10^{12} by dry-air mole fraction) yr^{-1} (~5% yr^{-1}) since 1996 (Fig. 2.18b).

The concentration of 320 ppb N_2O in 2005 has added a radiative forcing of around 0.17 W m^{-2} over the preindustrial N_2O concentration of around 270 ppb (Fig. 2.18a). Atmospheric N_2O is also a major source of stratospheric nitric oxide (NO), a compound that helps to catalytically destroy stratospheric O_3.

The atmospheric concentration of SF_6 has grown due to its use as an electrical insulator for power transmission throughout the world. Its global mean concentration was 5.75 ppt at the end of 2005 (Fig. 2.18b). While total radiative forcing of SF_6 from preindustrial times to the present is relatively small (0.003 W m^{-2}), its long atmospheric lifetime, high atmospheric growth rate, and high global warming potential are a concern for the future.

v) Halocarbons—R. C. Schnell[81]

Concern over stratospheric ozone depletion has restricted or eliminated production of many halocarbons. The phase out of human-produced halocarbons was the result of the 1987 Montreal Protocol on Substances that Deplete the Ozone Layer. As a result of these efforts, mixing ratios of many ozone-depleting gases have been declining at Earth's surface in recent years; this decline continued in 2005 (Fig. 2.19). NOAA/Earth System Research Laboratory (ESRL)/Global Monitoring Division (GMD) measurements from around the globe show that tropospheric mixing ratios of CFC-12, the longest lived and most abundant human-made ozone-depleting gas in the atmosphere, peaked within the last few years (Fig. 2.19a).

Those data also show that mixing ratios of some halogenated gases continue to increase globally (Figs. 2.19a–d). The most rapid increases are in HCFCs and HFCs, which are chemicals commonly used as replacements for chlorofluorocarbons (CFCs), halons, and other ozone-depleting gases. Although HCFCs contain chlorine (Cl) and deplete O_3 with a reduced efficiency compared to CFCs, HFCs do not participate in O_3-destroying reactions.

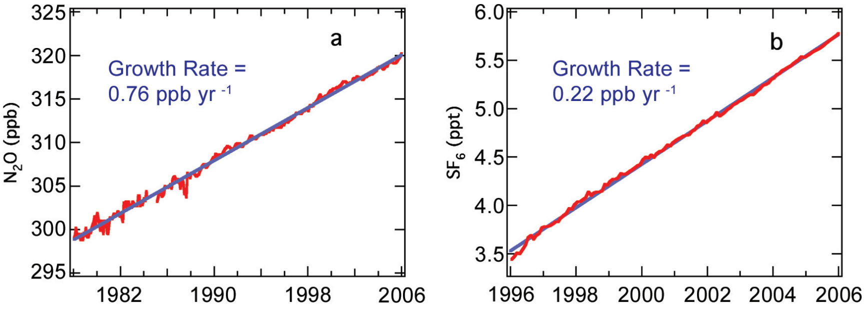

Fig. 2.18. (a) Global atmospheric N_2O from the NOAA/ESRL in situ and flask network (red) has increased with a linear growth rate (blue) of 0.76 ppb yr^{-1} from 1978 to the end of 2005. (b) Global atmospheric SF_6 from the NOAA/ESRL in situ and flask network (red) has increased at a linear rate (blue) of 0.22 ppt yr^{-1} from 1996 to the end of 2005.

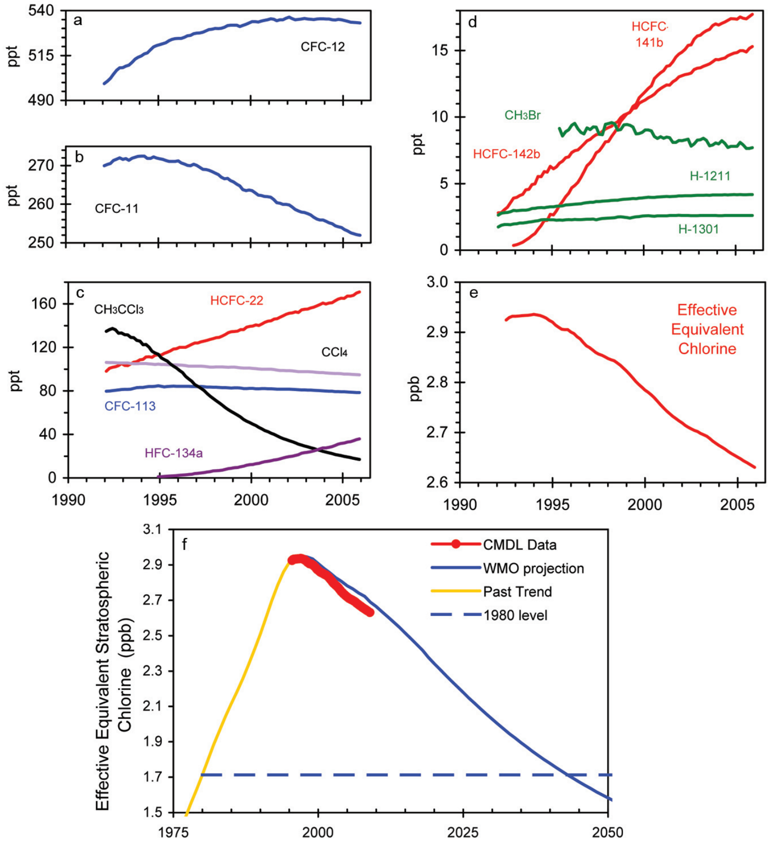

FIG. 2.19. (a)–(d) Changes in global mean tropospheric mixing ratios (ppt) of the most abundant CFCs, HCFCs, HFCs, chlorinated solvents, and brominated gases, calculated from atmospheric measurements made at remote sites in both the NH and SH. [Source: NOAA/ESRL/GMD cooperative air sampling network] (e) Secular changes in atmospheric equivalent chlorine (EECl; ppb). (f) Recent changes in effective equivalent stratospheric chlorine (EESC) observed by the NOAA/GMD global network relative to the secular changes observed in the past. EESC is derived from EECl by adding 3 yr to represent the lag associated with mixing air from the troposphere to the middle stratosphere (updated from Montzka et al. 2003a,b). [Courtesy: S. A. Montzka, J. H. Butler, T. Thompson, D. Mondeel, and J. W. Elkins, NOAA/CMDL]

Increases in HCFCs have slowed notably in recent years. By mid-2005, the Cl in the three most abundant HCFCs amounted to 217 ppt, or 8.0% of all Cl carried by long-lived halocarbons. Mixing ratios of HFC-134a, the most abundant HFC in the global background atmosphere, increased nonlinearly in the 1990s. From 2001 through 2005, however, it has increased in the global troposphere at a fairly constant linear rate of 4.2 ppt yr^{-1}. Concern over increases in HFCs is largely due to their efficiency as absorbers of infrared radiation.

The influence of these disparate trends on future levels of stratospheric ozone can be gauged roughly from a sum of Cl and bromine (Br) in long-lived halocarbons, provided the enhanced efficiency for Br to destroy ozone is considered. This sum is expressed as effective equivalent chlorine (EECl; Fig. 2.19e), and is derived from surface-based measurements. EECl provides an estimate of the O_3-depleting power of the atmosphere a few years in the future, when air at Earth's surface will have become mixed into the stratosphere.

Observations indicate that the EECl content of the lower atmosphere has declined at a mean rate of 26 ppt yr^{-1} since its peak in 1994. Scenarios projecting future halocarbon mixing ratios have been derived elsewhere based upon full compliance with the fully amended and revised Montreal Protocol and our understanding of atmospheric lifetimes of these gases (Montzka et al. 2003b). These analyses suggest that it will take 40–50 years for EECl to decline to the levels present in 1980, before O_3 depletion was first observed. This 1980 level is notable, given that one might expect nearly full recovery of stratospheric ozone once the atmospheric EECl returns to this level. The time frame for O_3 recovery will depend upon other factors as well, such as stratospheric temperatures and atmospheric aerosol loading. Nonetheless, the declines in EECl from 1994 to the present time represent a significant drop in the atmospheric EECl burden. As of 2005, EECl had declined 20% of the way back to the 1980 level (Fig. 2.19f).

Changes in the direct radiative influence of long-lived halocarbons can be estimated from observed changes in atmospheric mixing ratios with knowledge of trace-gas radiative efficiencies. Such an analysis suggests that the direct radiative forcing of these gases was still increasing in 2005, though at a much slower rate than observed from 1970 to 1990.

3. GLOBAL OCEANS—J. M. Levy[47] and K. A. Shein[82], Eds.

a. Overview—K. A. Shein[82]

Recent decades have seen a marked increase in our knowledge of the coupled ocean–atmosphere system, although as is discussed, it is only through a number of relatively new or planned ocean-monitoring ac-